NTNU – Trondheim
Norwegian University of
Science and Technology

Thermal Dependence of Shear Banding in Zr70Ni16Cu6Al8 Bulk Metallic Glasses

David Dominikus Eide
Brennhaugen

Materials Science and Engineering
Submission date: September 2014
Supervisor: Lars Arnberg, IMTE
Co-supervisor: Yoshihiko Yokoyama, IMR, Tohoku University

Norwegian University of Science and Technology
Department of Materials Science and Engineering

Thermal Dependence of Shear Banding in $Zr_{70}Ni_{16}Cu_6Al_8$ Bulk Metallic Glasses

David Dominikus Eide Brennhaugen

September 2014

Department of Materials Science and Engineering, NTNU
Institute for Materials Research, Tohoku University

Supervisor 1: Professor Lars Arnberg
Supervisor 2: Professor Yoshihiko Yokoyama

Declaration

I hereby declare that the work presented in this document has been performed independently and in accordance with the rules and regulations of the Norwegian University of Science and Technology (NTNU) and directions given by the supervising professors.

Sendai 29.09.2014

David Dominikus Eide Brennhaugen

Preface

The present work was done as a master thesis for 30 credits during the 10th semester of the MSc course in Materials Science and Engineering at NTNU, Norway. The work is a result of collaboration with Tohoku University, Japan, where all practical and theoretical work has been conducted.

I wish to thank my two co-supervisors, Yoshihiko Yokoyama, Tohoku University, for invaluable guidance in both theoretical and practical parts of the work with bulk metallic glasses, and Lars Arnberg, NTNU, for help in writing this project and making the collaboration a possibility.

I would also like to thank technicians Murakami, Narita and Endo, Tohoku University, for help with XRD- and SEM analysis and machining, as well as Dehlia Eide Brennhaugen for advice with writing style and formalities. The staff at the machine shop of the Institute for Materials Research at Tohoku University have also been of invaluable help in manufacturing tensile specimen.

This thesis is a thematic continuation of a project work on BMG production done in the previous semester. Some parts of the text in this work have been taken from this previous project.

Abstract

$Zr_{70}Ni_{16}Cu_6Al_8$ bulk metallic glass samples were cast and prepared for tensile testing. Tensile tests were done at temperatures 77 K, 150 K and 295 K, over a range of effective strain rates between 10^{-5} and $10^{-1}/s$ in order to assess the dependence of plastic deformation through shear band sliding on the aforementioned factors.

A strong temperature dependence was found, with maximum shear band sliding distance at 150 K. The sliding distance was also found to increase with lowered strain rates. The temperature dependence is likely to stem from increased heat dissipation suppressing a decrease in viscosity, while the strain rate dependence stems from a decrease in energy supply rate.

Shear bands appeared at higher stresses at lower temperatures, resulting in larger elastic domains and higher ultimate tensile stresses. A mechanism where heat dissipation suppresses the formation of shear bands at low stresses was proposed.

Sammendrag

$Zr_{70}Ni_{16}Cu_6Al_8$ bulk metallisk glass ble støpt og behandlet for strekktesting. Det ble gjort strekktester ved temperaturene 77, 150 og 295 K, over en rekke strekkhastigheter mellom 10^{-5} og $10^{-1}/s$ for å utforske sammenhengen mellom plastisk deformasjon ved skjærbåndglidning og de nevnte faktorene.

En sterk temperaturavhengighet ble funnet, med maksimal glideavstand ved 150 K. Glideavstanden økte også ved lavere strekkhastigheter. Temperaturavhengigheten stammer sannsynligvis fra økt varmedispersjon ved lave temperaturer, noe som hindrer en lokal senkning av viskositeten, mens strekkhastighetsavhengigheten stammer fra redusert energitilførsel ved lav hastighet.

Skjærbåndene ble dannet ved høyere spenning ved lav temperatur, noe som førte til et forstørret elastisk område og høyere maksimal spenning. Det ble foreslått at høy varmedispersjon hindrer dannelsen av skjærbånd ved lave spenninger.

Contents

Chapter 1

Introduction

Since metallic glasses were discovered in 1960 [1], their applicability has evolved rapidly alongside their development. Early limitations in sample size have been pushed back, with the maximum thickness increased from the order of 100 μm[1] to above 70 mm[2]. Alloys that can be produced in dimensions larger than 1 mm are called bulk metallic glasses (BMG), and include the alloy studied in the present project. BMGs differ from conventional metals on the atomic scale. Where metals normally crystallise during solidification, the atoms in a BMG remain largely unordered. This gives an atomic structure resembling that of the liquid state, with no large scale repeating patterns. The alloys' unique structure gives rise to properties making them attractive choices in a number of fields, where a combination of high strength, elasticity, resistance to wear, and in some cases biocompatibility, is desirable. Current uses include sporting goods, corrosion and abrasion resistant coatings, cutlery, medical and electrical equipment, while further uses, amongst others in medical implants, are being developed.

The aim of this work is to study the thermal activation of shear banding during tensile testing of the BMG $Zr_{70}Ni_{16}Cu_6Al_8$, which is a well known glass former [3]. Samples were produced by the same technique as previously reported [4], by first making alloy ingots, which were then cast into rods by tilt casting[5]. The rods were machined into tensile specimen. Tensile tests were performed at room temperature, at the temperature of liquid nitrogen and approximately 150 K. X-ray diffraction was used to gage the quality of the samples, while SEM imaging was used to study the individual fracture surfaces after testing.

Chapter 2

Background

2.1 Bulk Metallic Glass

Metals usually crystallise when transforming from liquid to solid state. However, some can be forced to retain a liquid-like, amorphous structure if cooled sufficiently fast, as was first shown by Klement et al. in 1960[1]. Due to the structural similarities with organic and oxide glasses, such materials are called metallic glasses. The required cooling rate, coupled with a finite heat conductivity, sets upper limits to the macroscopic dimensions of these metals. Early research yielded only thin ribbons of less than 100 μm thickness, but alloys were soon discovered that could be cast into glassy rods with a diameter of more than 1 mm [6]. These materials are called bulk metallic glasses (BMG). Recently, the maximum diameters have been increased to above 70 mm [2], making the choice of BMG alloys more viable for constructional purposes.

Transformation from liquid to glass does not give a discrete jump in hardness like crystallisation does. Instead, what can be observed is a gradual increase in viscosity with decreasing temperature, until liquidity is no longer observable on an experimental time scale. Due to its ambiguity, several definitions of the glass transition are in use. One gives a cut off value for the solid glassy state, arbitrarily set at viscosity higher than $10^{12} Pas$[7]. The temperature at which a supercooled liquid reaches this viscosity is often used to define the glass forming temperature, T_g. As metallic glasses are metastable, there are also changes in heat capacity related to the glass formation. This change is measurable by differential scanning calorimetry,

and has therefore been used as an opposing definition of T_g[8]. Due to the lack of a direct relation to structural change, this is labelled a second order phase transition, as opposed to crystallisation, which is a transformation of the first order. While a supercooled liquid is prevented from crystallisation only by kinetics, meaning it would crystallise given enough time, a glass, being metastable, is in a state of a local energetic minimum. This implies that the glass can exist indefinitely, as long as no energy is supplied.

During crystallisation, most materials experience a significant volume change. Because there is no distinct change in structure during glass formation, BMGs do not experience this to the same degree[9]. This makes it easy to cast BMG materials directly into the desired shape, reducing need for further machining. This is an advantage in industrial applications, because it reduces costs and enables the production of complex directly cast shapes.

BMGs have some traits which make them easily identifiable during analysis. As opposed to crystalline materials, BMGs do not produce a sharp characteristic spectrum during XRD analysis. Instead, smooth waves can be found in the pattern, corresponding to short range ordering in the amorphous alloy[3]. The absence of sharp XRD peaks is therefore a simple way to identify a glassy material. It has also been shown that the heat produced during deformation of BMGs considerably increases local temperature in the deformed area[10]. This results in a local decrease in viscosity, essentially giving a viscous liquid flow along the fracture surface. The flow can be observed later by studying the fracture surface, which will show a vein pattern where the liquid has dried after fracture. An example is shown in figure 2.1.This is useful in identifying glassy phases, as this phenomenon will not happen in crystals.

2.2 Glass Forming Ability

The glass forming ability (GFA) is the ease with which an alloy can obtain a glassy state, and is represented by the critical cooling rate (R_c), the lowest cooling rate which allows glass formation. R_c has been studied in relation to several characteristic temperatures of a metallic glass. The liquidus temperature (T_l)of the alloy is important, because it is beneficial to reach as slow kinetics as possible while still in a stable liquid phase. Before solidifying, a melt exists in a supercooled liquid state when brought beneath T_l. If the supercooling is sufficiently low, kinetics stop crystallisation from happening

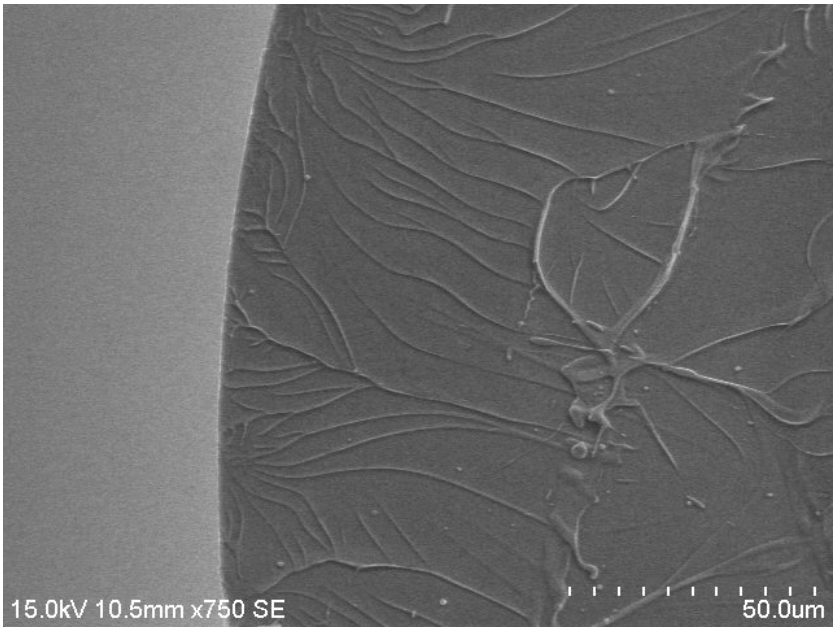

Figure 2.1: Vein pattern, as observed after viscous flow during fracture of a BMG.

within a relevant time frame. This point is called the crystallisation onset temperature(T_x), due to the fact that it is measured by heating slowly from the glassy state into the liquid state. At T_g the alloy changes from the state of a kinetically stabilised liquid to an energetically metastable amorphous solid.

A large gap between T_g and T_x generally corresponds to a lower R_c. At the same time, a small gap between T_g and T_l is also desirable. These relations have given rise to several attempts at mathematical prediction of R_c based on the characteristic temperatures[11][12][13].

Since the whole alloy needs to be cooled faster than R_c, high thermal conductivity is also beneficial. Good glass formers do however tend to have a decreased thermal conductivity[14][15], so the GFA is in practice a trade-off between low R_c and high conductivity. Together, R_c and thermal conductivity set limits for the maximum dimensions of a given BMG, which are very relevant for industrial applications of the materials.

To predict alloys with a high GFA, three empirical ground rules have been set[16]: Several different elements are required, usually at least three; there

should be an atomic size mismatch of at least 12 % between the largest and smallest constituents; there should be a negative heat of mixing between the elements.

When introducing alloying elements of significantly different radii from the matrix metal, severe lattice stresses would be induced if these alloying elements took up either interstitial or substitutional positions[17]. This reduces the energetic benefit of the crystalline phase, giving an increased aversion to crystallisation with an increased disparity in radius. BMGs are normally made by mixing smaller alloying elements into a matrix of larger atoms[18], but similar lattice stresses can be achieved by mixing larger atoms into a smaller matrix, possibly enabling glass formation in the latter case as well[17].

With alloying elements of different sizes put together in the structure, the overall density of the material increases. This might in turn increase thermal stability of the melt through a rise in viscosity[18]. The increased viscosity reduces the diffusivity of the constituent elements, practically obstructing diffusion into long range order during solidification. The ease of entering a supercooled liquid state without crystallisation, is also increased by using alloy compositions near to deep lying eutectics, where low temperatures, and therefore slow kinetics, might be reached while still in equilibrium [15]. This corresponds well with the aforementioned tendency for a smaller gap between T_g and T_l to increase the GFA.

The last ground rule, requiring a negative heat of mixing, inhibits phase separation of the alloying elements during cooling. This ensures the continued benefit of the size disparity of the atoms while going into the supercooled liquid state.

2.3 Mechanical Properties

Compared to their crystalline counterparts, metallic glasses show a considerable increase in both strength and toughness[15]. For instance, a glassy alloy $Al_{85}Ni_6Fe_3Gd_6$, was tested to an ultimate tensile strength of 1280 MPa [19], which is well into the realm of steels, and more than twice what can be expected from hardened commercial aluminium alloys. For Fe based BMGs, fracture strengths of over 3000 MPa have been reported[16].

Generally, BMGs exhibit high elasticity, but very low plasticity. An elastic region of up to 2 % is not uncommon[16], but the low plasticity means sud-

den catastrophic failure can occur only shortly after yielding. Therefore the alloys need to be applied with care for constructional purposes. Currently, work is being done to increase plasticity amongst others through making composite materials[20]. Related to the high strength, BMGs also show very high hardness values, making them attractive in applications requiring high resistance to abrasive wear[9].

The fact that metallic glasses consist of one continuous amorphous structure, yields several advantages. Solidification without diffusion keeps the structure homogeneous, because there is no driving force for segregation. This negates problems which arise in conventional crystalline metals, where grain boundaries can be the source of both corrosion and embrittlement.

2.4 Shear Banding

The primary tensile plastic deformation mechanism for BMGs at temperatures significantly lower than T_g is highly localised deformation in so called shear bands[21]. A shear band is an angled surface cutting through the specimen. Elongation of the sample will happen in the form of sliding along this surface, as shown in figure 2.2. Typically, there will be some amount of sliding along the shear band, before a final, sudden rupture of the remaining area. The final rupture will also happen along the same shear band. Studying the fracture surface, two distinct zones can be identified: A featureless zone, where sliding happened, and an area covered in the characteristic vein pattern after rupture of a BMG. These two zones can easily be distinguished in figure 2.3.

The mechanism for shear banding has been shown to consist of a localised increase in temperature, giving lowered viscosity, which results in a viscous flow along the shear band [22][10]. It has also been proposed that an increase in free volume, as well as a breaking up of short range ordering contribute to further decrease local viscosity[10]. The exact angle between the tensile loading direction and shear bands is material specific [23]. The shear band angle for the alloy studied in this work has previously been reported to be 52° [10].

At the onset of plasticity, several shear bands will usually form. With increased strain, most will become dormant, while one dominant band will propagate to accommodate remaining strain. Some times, several larger shear bands can be seen crossing each other in the fracture surface of a

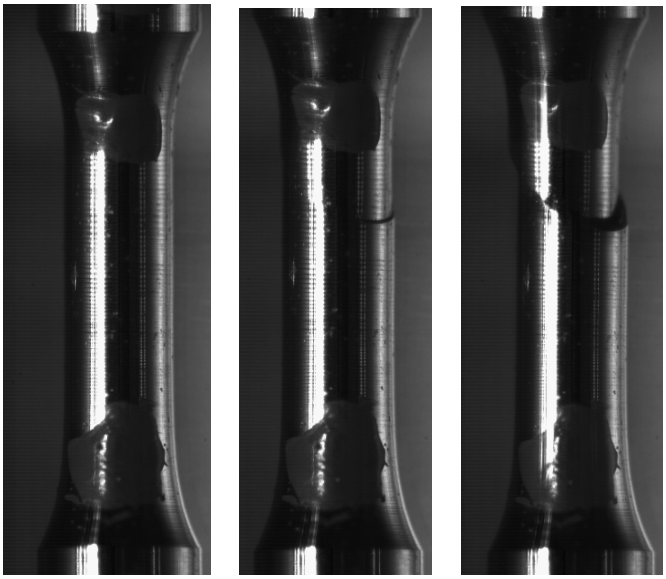

(a) Before shear banding (b) Early shear banding (c) Right before fracture

Figure 2.2: Overview of the progression of a shear band during tensile loading of a ZNCA specimen. Before shear band initiation (a), early during shear band sliding (b) and right before final fracture (c).

specimen, as shown i figure 2.4, where a secondary shear band can be seen protruding at an angle from the surface of the dominant one.

Contrary to many crystalline metals, BMGs do not show any work hardening during plastic deformation. Rather, they exhibit localized softening in the shear band region, making the plastic deformation unstable[24]. Due to the weakening contributions of the free volume generation and the short range disordering, this softening is at least partly permanent, even after removal of stress [25], which means that deformation will continue in the same location if a sample is de- and re-loaded.

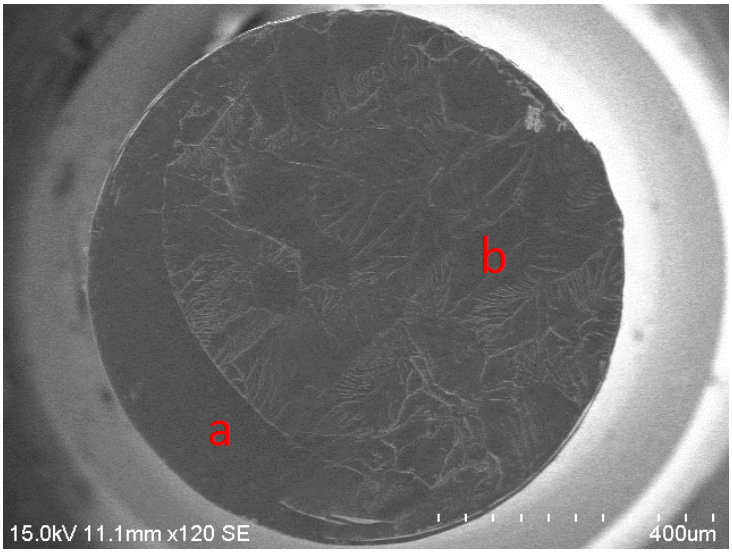

Figure 2.3: Overview of fracture surface from sample shown in figure 2.2. Shear band sliding area (a) is easily distiguishable from rupture area (b).

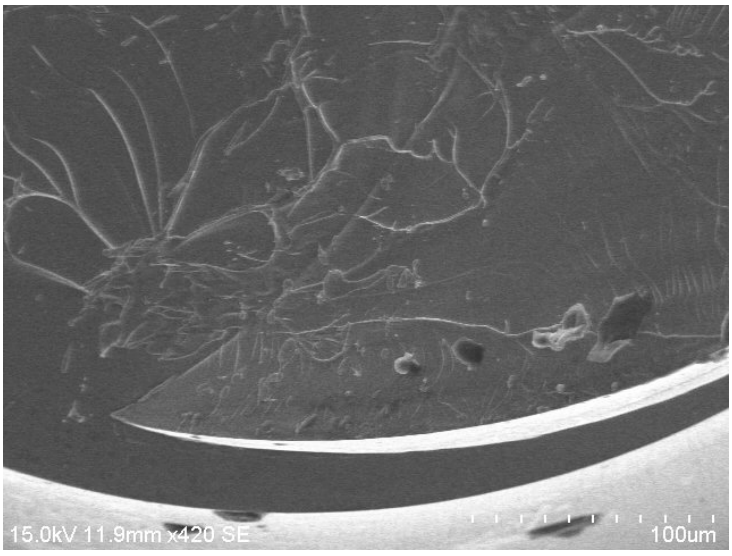

Figure 2.4: Easily distinguishable intersection between two major shear bands in the fracture surface of ZNCA tensile specimen.

2.5 $Zr_{70}Ni_{16}Cu_6Al_8$

The alloy studied in this project is $Zr_{70}Ni_{16}Cu_6Al_8$(ZNCA). For the included elements, the eutectic composition, which gives the highest GFA, is found at $Zr_{54}Ni_6Cu_{30}Al_{10}$. Being hypoeutectic, ZNCA does not possess an impressive GFA. It is however designed specifically with other properties in mind: In order to increase plasticity, an alloy with reduced Young's modulus and increased Poisson's ratio is desired. This is achieved by the reduction of Al and Cu content, substituting it for Zr[3]. Another feature of this composition is its high resistance to stress corrosion cracking[16].

During tensile testing, ZNCA has previously shown a correlation between plasticity and strain rate. At a strain rate of $10^{-4}s^{-1}$, no plasticity was observed at room temperature. At a higher strain rate of $1.5 \cdot 10^{-1}s^{-1}$, 2.8 % plastic strain has been observed. The ability to accommodate higher plastic deformation at high strain rates, has also been shown to depend on the cooling rate of the glass, with a higher cooling rate giving higher plasticity[3][26]. During cryogenic trials at 133 K, the alloy was found to have significantly increased plasticity, especially at lower strain rates[27]. A summary of some important properties can be found in table 2.1.

2.6 Tilt Casting

When casting BMG samples, several challenges have to be overcome. Because any crystalline nuclei in the melt can inoculate crystallisation during cooling, a homogeneous melt with no solidified particles is imperative. Cooling must also be avoided while pouring the melt into the mould for the same reason, while a relatively high cooling rate is required after entering the mould. In order to accommodate these requirements, a tilt casting system with twin arc melting torches was used for producing ZNCA rods[5].

In this system, the alloy is placed on a horizontal hearth, where it is heated by two arc melting torches. A mould is fastened to one side of the

Table 2.1: Some important properties of the BMG alloy $Zr_{70}Ni_{16}Cu_6Al_8$. [3][26]

E[GPa]	ν	ϵ_e[%]	σ_y[**MPa**]	T_l[**K**]	T_x[**K**]	T_g[**K**]
69	0.393	2.2	1500	1293	698	630

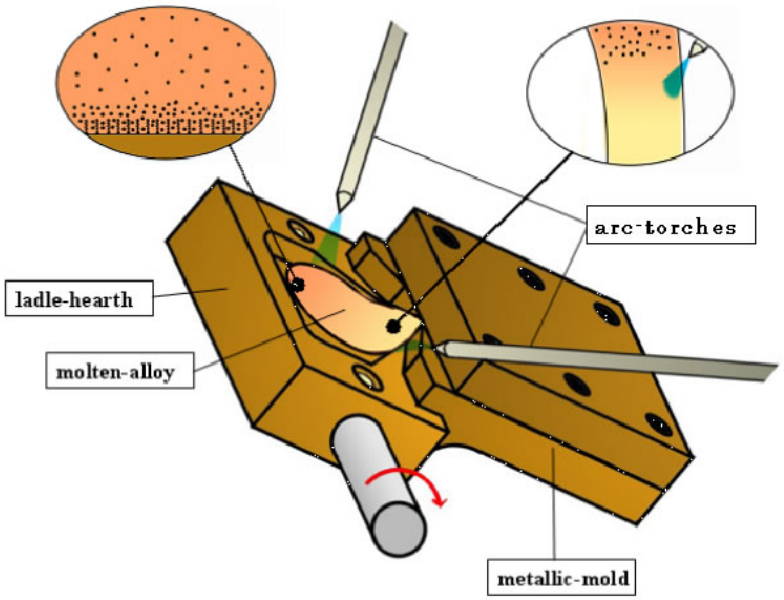

Figure 2.5: Sketch of the tilt casting system equipped with dual electric arc torches, used in this project. Courtesy of Yoshihiko Yokoyama[28].

hearth. Both the hearth and the mould can be tilted together, allowing the molten alloy to flow from the former into the latter. By careful placement of the alloy and the torches in relation to the rotational axis of the system, continued heating of the melt can be assured during pouring. Flow speed can be controlled through the tilting speed and angle. This system has been shown to give a noticeable improvement in cast quality, compared with a single torch system [5]. A sketch detailing the system is shown in figure 2.5, courtesy of Yoshihiko Yokoyama.

The hearth and mould are both made of copper, and are connected to a water cooling system, in order to prevent diffusion between the alloy and the hearth, as well as to supply cooling during solidification. The casting is done in an Ar atmosphere in order to avoid oxidation. To ensure the quality of the atmosphere, two pure Zr ingots are placed on the hearth, alongside the alloy. These are heated before the alloy is melted, helping in cleaning the atmosphere due to their high affinity to oxygen.

Chapter 3

Experimental Work

3.1 Master Alloy Production

Alloy ingots of 20-30 g were produced. The separate alloying elements were weighed out by an automatic weighing machine. An arc melter (Custom built, Diavac Limited, model no. 310-035-675), with a capacity of 22 ingots per batch, was used to melt the elements into ingots. The chamber was evacuated to the order of 10^{-4} Pa, before an Ar atmosphere was introduced. A tungsten electrode was used to heat the elements and melt them into ingots. The ingots were then turned and heated again. This was repeated four times. In order to achieve high homogeneity in the molten alloy, convection was induced by a combination of different amperages, both at alternating and direct current. The exact proceedings of the melting are presented in Table 3.1. After cooling, the ingots were removed from the melter and crushed into smaller pieces of 5-8 g, to give more precise control over the amount of alloy used for later casting. The pieces of master alloy were stored under vacuum conditions.

3.2 Tilt Casting

A Nissin Giken manual tilt casting machine with two torches (Model no. 107-000009437-000) was used to create circular cast rods with 3.5 mm diameter and 8.5 cm length. For each cast, between 11.6 and 13 g of master alloy was used. The placement of the alloy on the hearth, relative to the rotational axis, the electrodes and the mould is illustrated in Figure 3.1(a). A combination

Table 3.1: Exact program for the automatic arc melting machine.

Round	**Mode**	**Amperage [A]**	**Frequency [Hz]**	**Time [s]**
1	DC	320		120
	AC	250-400	9	500
	DC	330		180
2	DC	300		60
	AC	250-380	9	180
	DC	330		60
3	DC	300		60
	AC	250-380	10	180
	DC	330		60
4	DC	300		60
	AC	250-380	11	180
	DC	120		180

of a rotary and a diffusion pump was used to evacuate the casting chamber to the order of 10^{-3} Pa, before an argon atmosphere was introduced. Two Zr ingots of around 4 g were heated at 100 A each for 60 seconds, in order to absorb remaining oxygen in the atmosphere. The metal was melted at 100 A with one torch, while the other still heated a Zr ingot. The electrodes were placed about 2 mm above the alloy, and positioned to induce convection in the melt, as illustrated in Figure 3.1(b). Both torches were then used to heat the alloy ingot for 90 seconds at 300 A each. The current was increased to 400 A on both torches for 10 seconds, before the hearth was tilted quickly to pour the molten alloy into the mould. The chamber was left to cool for five minutes before venting and extracting the completed rod, pictured in figure 3.2. Between the casting of each rod, the chamber, the hearth, the mould and the electrodes were cleaned with ethanol. The electrodes were also checked for damage or pollution, and exchanged if needed. After each casting, impressions of the resulting rod, as well as the proceedings of the casting, were recorded. Fractures, inclusions, deformations and surface texture were documented.

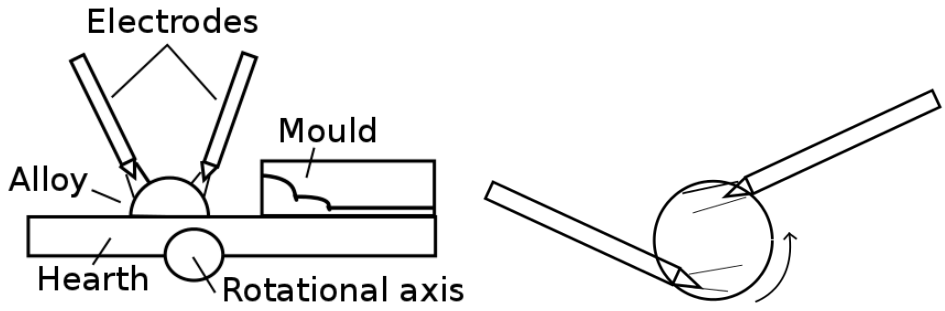

(a) Alloy placement (b) Electrode placement

Figure 3.1: Schematic showing the placement of alloy on the hearth, relative to the rotational axis and the mouth of the mould (a) and electrode positioning used to induce convection in melt (b).

Figure 3.2: A finished cast specimen after extraction.

3.3 Machining

Completed cast rods were sent to the machine shop at Institute for Materials Research at Tohoku University for machining into tensile specimen. The machined specimen were 28 mm long, with a 2.3 mm long, 0.8 mm diameter, gage area. On either side there was a 10 mm long area of M3x0.5 threading, for fastening the sample to the holder. Additionally, cylindrical samples, 6 mm long, 3 mm diameter, were made for use in XRD analysis. Figure 3.3 shows schematic sample placement in cast rods (a), schematic of tensile specimen(b) and actual samples (c).

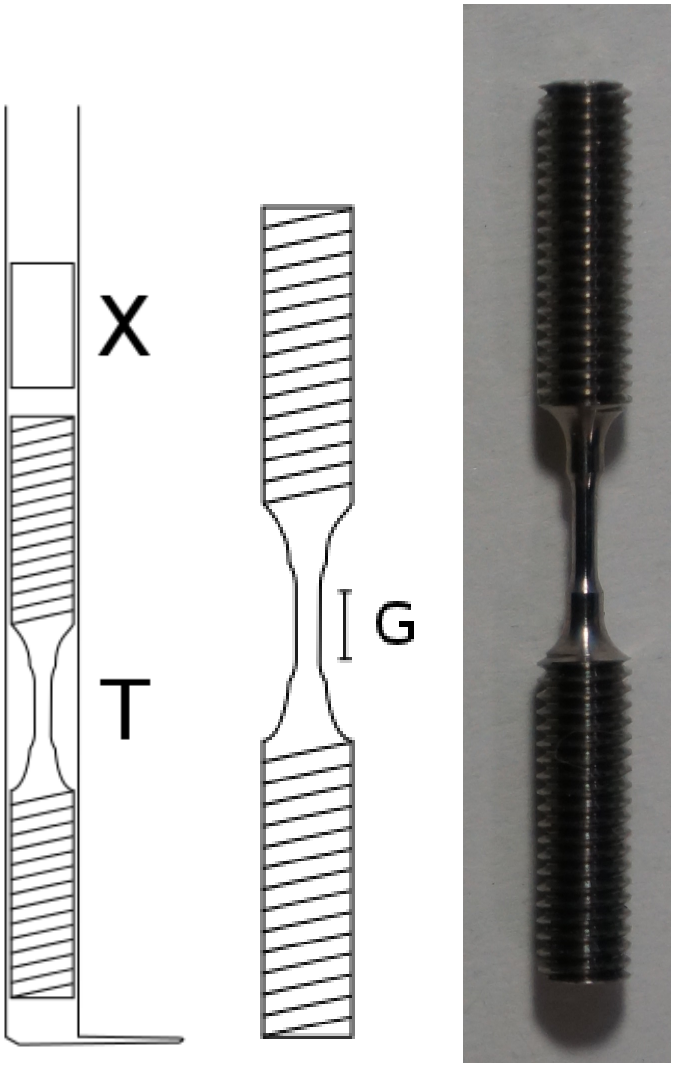

(a) Cut outs from cast rods (b) Sketch of tensile specimen (c) Actual tensile specimen

Figure 3.3: Schematic of how specimen were cut from cast rods, X=XRD sample, T=tensile sample (a), precise sketch of tensile specimen, gage area marked as G (b) and actual tensile specimen as received from machine shop (c).

3.4 Tensile Testing

Tensile testing was performed with a strain rate controlled Shimadzu AG-X machine, using a modified sample holder designed to allow the samples to be submerged in a cryogenic during testing. This was achieved by fastening the sample between the bottom of an outer tube and an inner rod, both suspended below the testing machine, as shown in figure 3.4 (a). A window in the outer tube allowed for in-situ observation using a high speed camera fitted to a microscope lens.

Nominal strain rates of $10^{-1}, 10^{-2}, 10^{-3} and 10^{-4}$ were applied at 295 K, 150 ± 20 K and 77 K. Effective strain rates were later calculated individually for the specimen, in order to account for elasticity in the equipment.

The gage area of each sample was polished in the axial direction, using 4000 grit Fujifilm Lapping Tape, in order to remove any potential fracture initiation points left from machining. An optical microscope (Shimadzu HMV-2 ADW) was used to confirm surface quality after polishing. A paint marker was used to mark the specimen with dots on either end of the gage area, in preparation for later motion tracking using the high speed camera, before the specimen was mounted in the holder. 20 N pre-load was applied to stabilise the specimen in front of the camera. The tensile testing program was then started at a specified strain rate.

For the low temperature tests, temperature control measures, as described in the subsequent section, were taken before starting the test. In the case of the highest strain rate tests, the desired rate was gradually but quickly approached, to avoid early fracture by jerking the specimen.

3.5 Temperature Control

A temperature control regimen using liquid nitrogen as a cryogenic was applied.

A custom made windowed quartz vial was installed around the sample holder. A plastic sponge lid, with holes for the sample holder, thermocouple and liquid nitrogen filling tube was placed on top of the vial. The filling tube and a YK-2000PK thermocouple were inserted. This setup is shown in figure 3.4 (b).

For 77 K tests, nitrogen was added until the sample holder was well submerged, and the thermocouple showed the correct temperature.

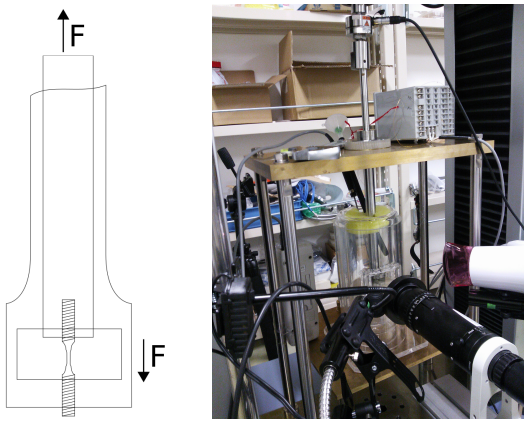

(a) Schematic of sample holder

(b) Mounted sample in quartz vial

Figure 3.4: Schematic of windowed, suspended sample holder (a) and mounted sample in tensile tester, with quartz vial, thermocouple and camera (b).

For 150 ± 20 K, nitrogen was added until the sample holder was suspended directly above the surface. Nitrogen evaporation, temperature and time were then monitored and plotted for 15 minutes, before evaporated nitrogen was refilled. Monitoring continued for 10 more minutes, before the tensile test was started exactly 25 minutes after first filling.

The plotted data from the temperature monitoring was then compared to calibration data, where an Au-Fe thermocouple (Delivered by Nilaco, monitored by a Chino DB1000 controller) had been soldered directly to the sample, and a relation between sample holder temperature and actual sample temperature had been found. Using this method, temperature could only be controlled to $150 \pm 20K$, while the set up was precise enough to measure the temperature within $\pm 5K$. A representation of the relation used to calculate sample temperatures is included as appendix A.

3.6 High Speed Camera

A Photron FASTCAM SA1.12 high speed camera, fitted with a Leica Z16 APO zoom lens, was set up to monitor the samples during tensile testing. Photron FASTCAM Viewer software was used together with a trigger sys-

tem measuring electrical resistivity through the sample, in order to precisely control what time frame to include in the video.

After testing, the video data was analysed using Track Eye Motion Analysis - Automotive software by Image Systems Motion Analysis. The distance between two points marked on the specimen were obtained as a function of time, and used to calculate exact values for Young's modulus and strain rate. Images from the software can be fount in appendix B.

3.7 SEM

Both fracture surfaces on all specimen were studied by SEM. Images were taken in secondary electron mode on a Hitachi S-3400N. The images were used to measure shear band sliding distance, as well as to study the mode of fracture for each specimen.

3.8 XRD

All samples were sent to be analysed by XRD by a technician at Tohoku University, in order to gage cast quality as related to individual performance in tensile testing. For each cast rod, a section adjacent to the one manufactured into tensile specimen was sent to be analysed. All diffractograms were taken with a Cu target, 2θ values of 20-100° and a resolution of 0.02° on a Rigaku Ultima IV X-ray Diffractometer.

Chapter 4

Results

4.1 Casting and Machining

A total of 70 cast rods of sufficient quality were produced and sent to machining. Brittleness due to incomplete vitrification resulted in the loss of 20 rods, which broke during machining. The remaining 50 rods received a rating from the machine shop, based on response to machining. An overview of the quality distribution is given in figure 4.1.

All the received tensile specimen were polished in the longitudinal direction using lapping tape, in order to remove any latitudinal cuts and lines from machining, which act as prime fracture nucleation spots. Several of the samples had marks that were too deep to be removed by polishing, without significantly changing the gage area diameter. An example is shown in figure 4.2, where latitudinal cutting lines, a pore from a cast defect and longitudinal lines from polishing can be seen.

Out of all the produced tensile specimen, 25 samples which were rated "good" by the machine shop and had satisfactory surface conditions were selected for further use in tensile testing.

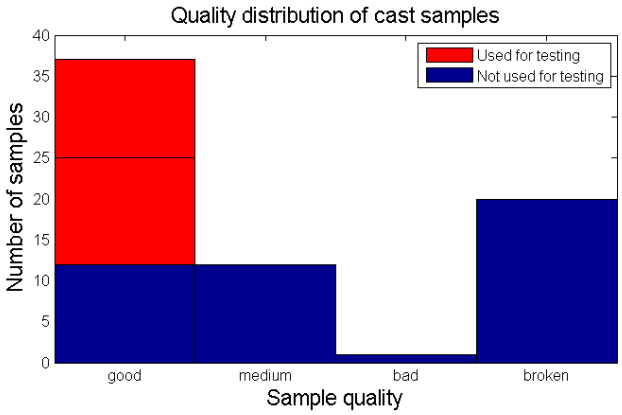

Figure 4.1: Histogram showing the quality distribution of submitted cast rods, as given by the machine shop.

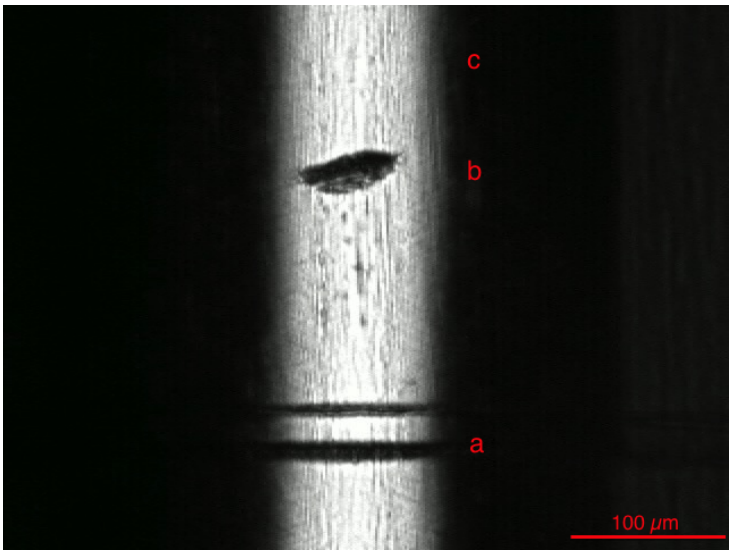

Figure 4.2: Optical micrograph showing cutting lines from machining (a), porosity from cast defects (b) and a well polished area with axial polishing lines (c).

4.2 Stress-Strain Curves

Tensile testing was done over four nominal strain rates ($10^{-1}, 10^{-2}, 10^{-3}, 10^{-4}/s$), at three different temperatures (77, 150, 295 K). Stress-strain curves obtained directly from the tensile testing machine showed severely inflated strain and strain rate values, as shown in figure 4.3 (a). The apparent curve also shows an incorrect curvature in the elastic region, due to relaxation in the sample holder. A regression was done based on data from TEMA video analysis software, in order to find actual strain rate and to calculate the correct Young's modulus, shown in 4.3 (b). Plasticity data from (a) was modified by a constant (variable between samples), in order to correctly fit the actual video data. Elastic and plastic data were finally combined, resulting in a calculated curve as shown in figure 4.3 (c). Based on these data corrections, actual strain rate turned out to differ significantly from the nominal strain. For the sample showed in figure 4.3, only 17% of the applied strain rate was conducted to the gage area.

Comparative graphs were made using one representative sample for each strain rate and temperature. The sample used for the test at 77 K, $10^{-4}/s$ strain rate, was produced externally by professor Yoshihiko Yokoyama, but was included in the comparisons due to faulty data on the equivalent specimen produced in this work. This sample is marked by dotted lines in all graphs where it is included.

Figure 4.4 shows stress-strain relation for room temperature at variable strain rate. Figures 4.5 and 4.6 show equivalent relation for 150 K and 77 K, respectively. Figures 4.7, 4.8, 4.9 and 4.10 show relation for comparative strain rates at variable temperatures.

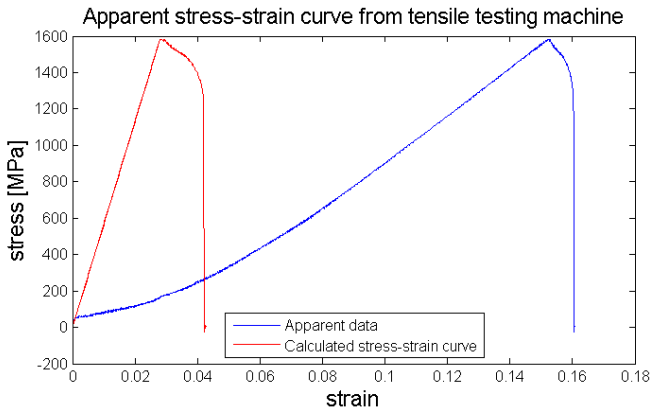

(a) Apparent stress-strain curve

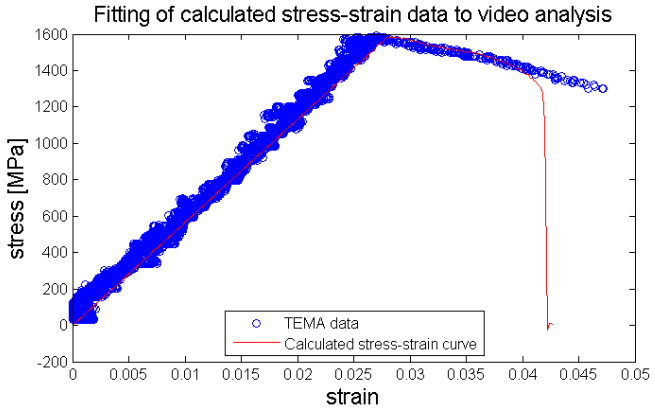

(b) Regression data

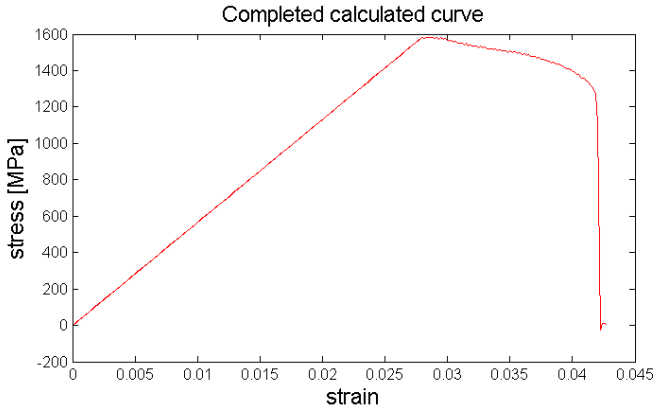

(c) Calculated stress-strain curve

Figure 4.3: Progression of calculation of stress-strain curves. Apparent curve from tensile testing machine (a), data fitting to image analysis data (b) and final calculated curve (c).

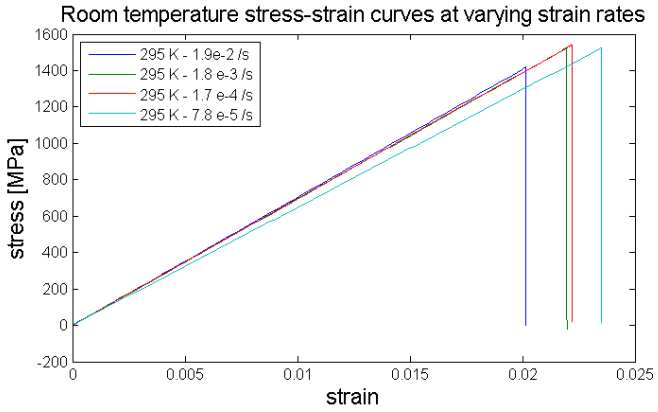

Figure 4.4: Comparison of stress-strain relation for tests at room temperature, over different strain rates.

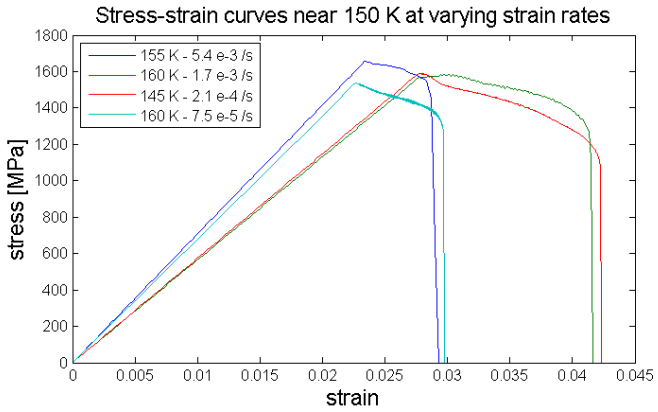

Figure 4.5: Comparison of stress-strain relation for tests around 150 K, over different strain rates.

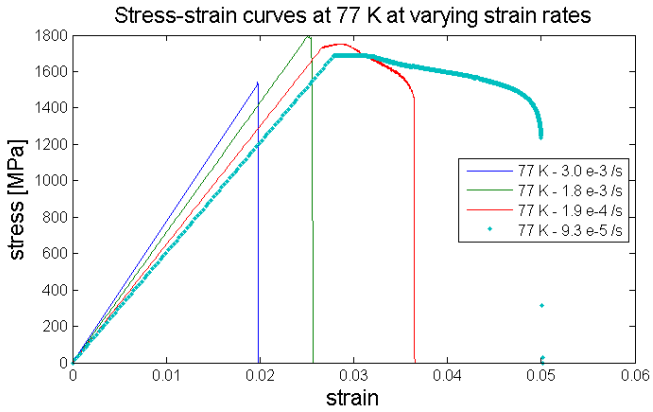

Figure 4.6: Comparison of stress-strain relation for tests at 77 K, over different strain rates. The sample marked by a dotted line was externally produced.

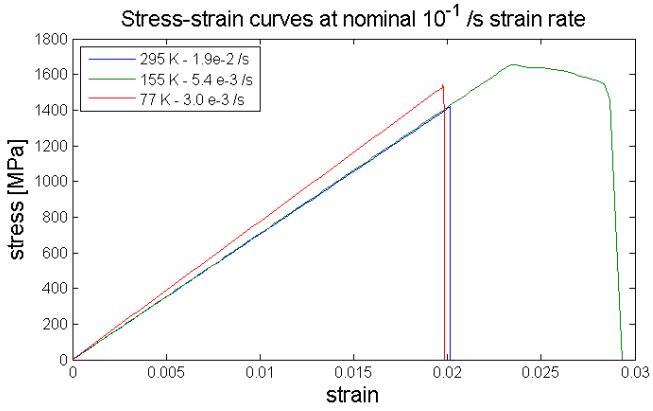

Figure 4.7: Comparison of stress-strain relation for tests at nominal strain rate $10^{-1}/s$ at different temperatures.

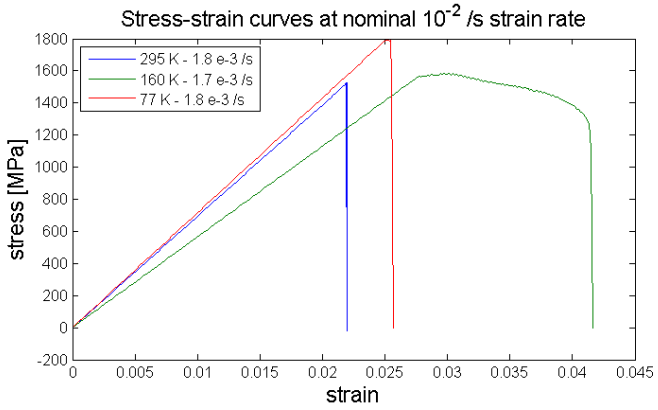

Figure 4.8: Comparison of stress-strain relation for tests at nominal strain rate $10^{-2}/s$ at different temperatures.

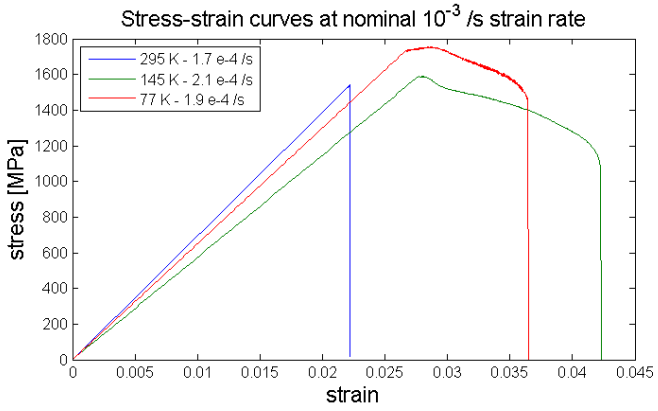

Figure 4.9: Comparison of stress-strain relation for tests at nominal strain rate $10^{-3}/s$ at different temperatures.

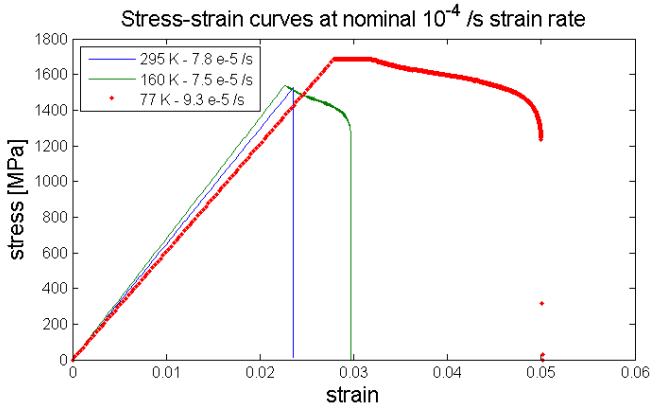

Figure 4.10: Comparison of stress-strain relation for tests at nominal strain rate $10^{-4}/s$ at different temperatures. The sample marked by a dotted line was produced externally.

4.3 Tensile parameters

Values derived from the tensile test results were used to search for correlations between testing parameters and specimen behaviour. In order to find general trends, data for different strain rates and temperatures were plotted together. Figure 4.11 shows a slight average decrease in Young's modulus with decreasing temperature. Figure 4.12 shows a clear increase in ultimate tensile stress (UTS) with decreasing temperature. Figure 4.13 shows an increase in Young's modulus with increasing strain rate, while figure 4.14 shows only a slight increase in maximum stress with increased strain rate.

When comparing maximum total strain, there is a marked increase at lower temperature, as shown in figure 4.15.

Average values for UTS, shear band sliding distance and elongation are tabulated in table 4.1.

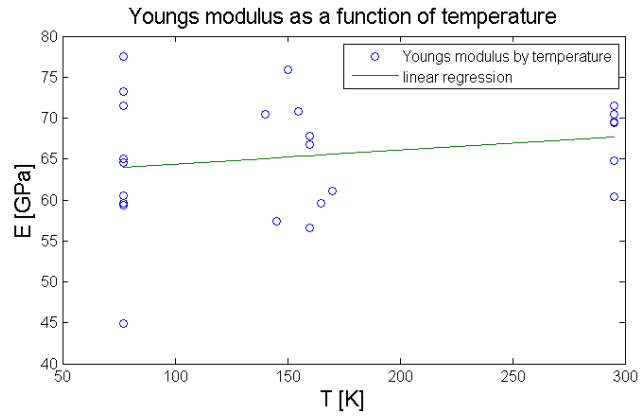

Figure 4.11: Young's modulus plotted as a function of testing temperature across all strain rates.

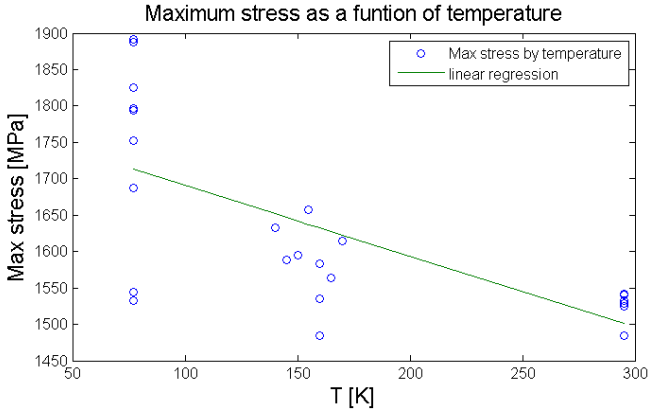

Figure 4.12: Maximum stress plotted as a function of testing temperature across all strain rates.

Table 4.1: Average UTS, shear band sliding distance and total strain for each temperature

	UTS [MPa]	Sliding distance [μm]	Total strain
295 K	1525,4286	68,142857	0,0225714
150 K	1583,8889	130,33333	0,0244444
77 K	1745,7778	85	0,0278667

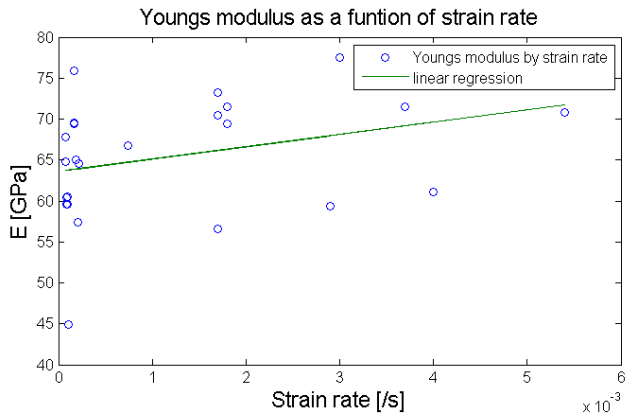

Figure 4.13: Young's modulus plotted as a function of applied strain rate across all testing temperatures.

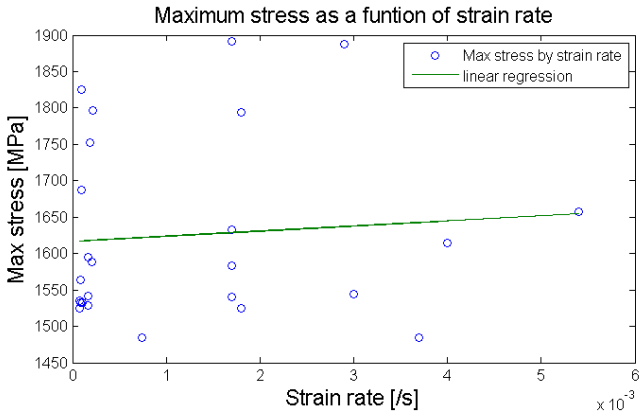

Figure 4.14: Maximum stress plotted as a function of applied strain rate across all testing temperatures.

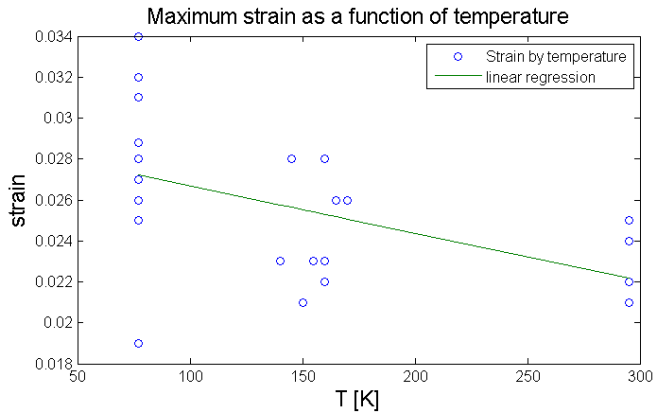

Figure 4.15: Maximum strain plotted as a function of testing temperature across all strain rates.

4.4 Fracture Surfaces

SEM was used to investigate the fracture surfaces of all specimen. Micrographs were taken in order to measure the sliding distance of the dominant shear band in each sample. Figure 4.16 (a) shows an overview micrograph, with marked sliding direction and displacement. Figure 4.16 (b) shows the measured displacement on the same sample.

An optical light microscope was used to measure the angles of the shear band, in order to calculate actual displacement in the sliding direction. The measured angle was found to be 54°, contrary to the previously reported 52°, as is shown in figure 4.17. This measurement was found to be consistent between the samples. Sliding distance measurements for all samples were recorded and compared. Sliding distance as a function of testing temperature is shown in figure 4.18, where a slight increase in distance with lowered temperature can be observed. Figure 4.19 depicts sliding distance as a function of strain rate, and shows a clear increase in sliding distance with decreased strain rate.

Shear band sliding distance was also used together with the angle information to calculate the actual plastic strain that occurred due to shear band sliding. Plastic strain as a function of tensile testing temperature and as a function of strain rate are shown in figures 4.20 and 4.21 respectively.

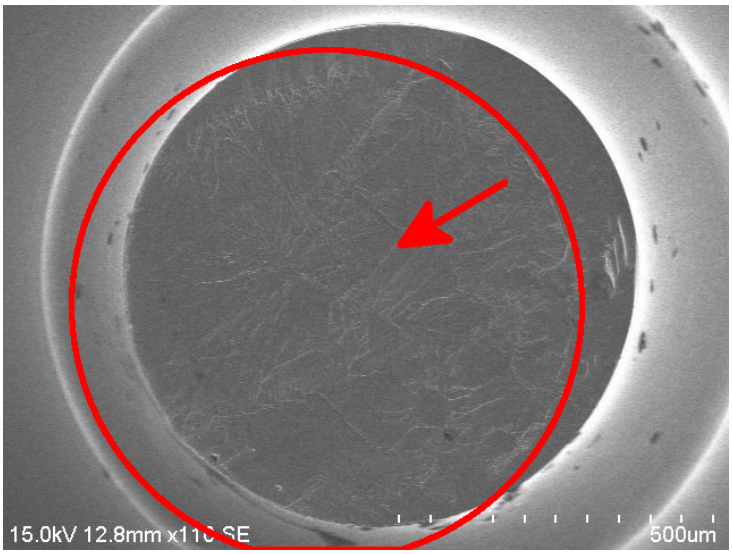

(a) Sliding displacement

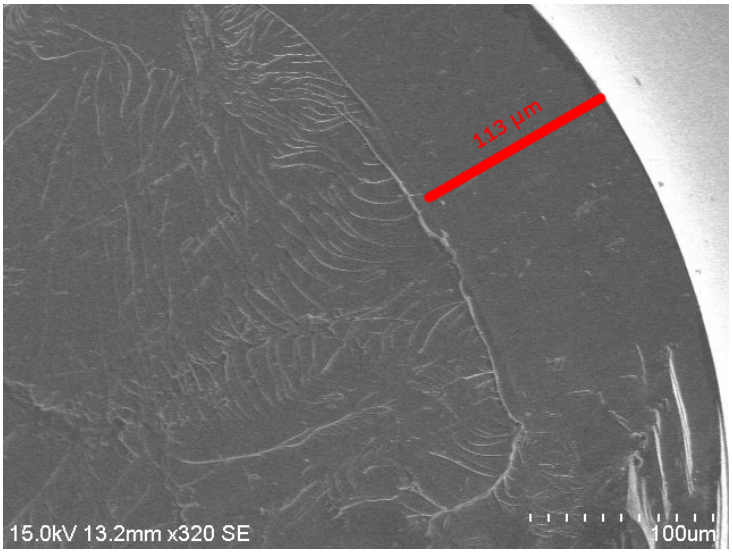

(b) Measured displacement

Figure 4.16: SEM micrographs showing sliding displacement from shear banding. Overview picture with marked sliding direction and displacement (a) and measured displacement (b).

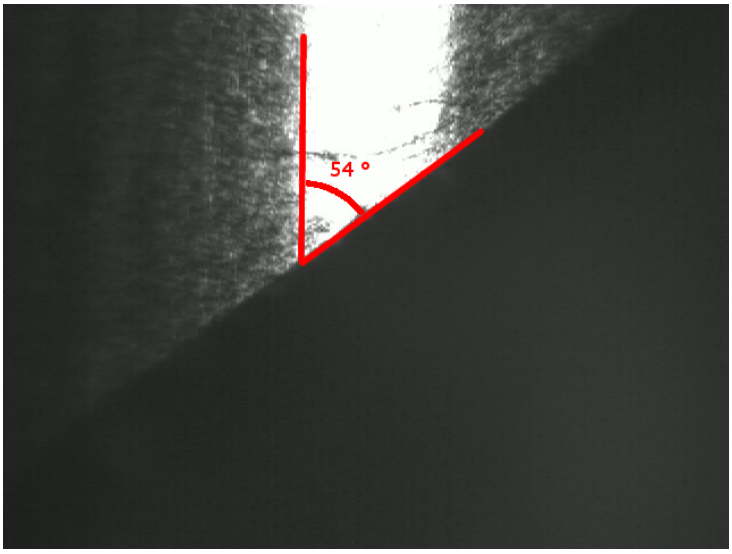

Figure 4.17: Measured shear band angle, using optical microscope

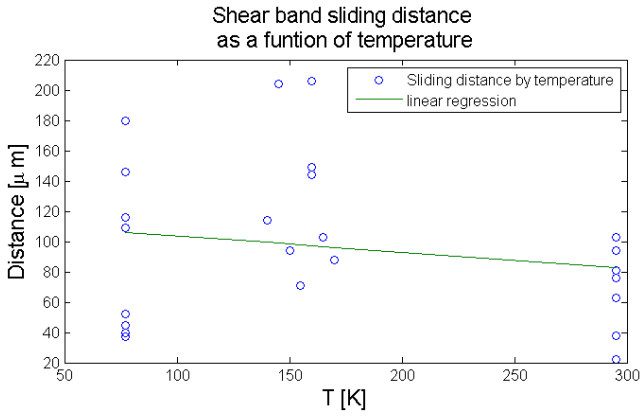

Figure 4.18: Sliding distance as a function of tensile testing temperature.

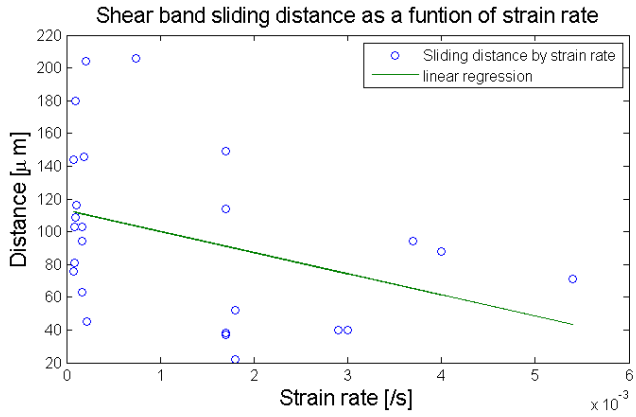

Figure 4.19: Sliding distance as a function of strain rate.

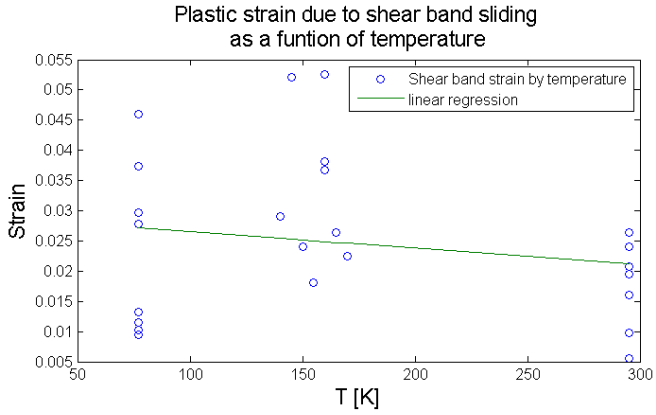

Figure 4.20: Plastic strain from shear band sliding as a function of testing temperature.

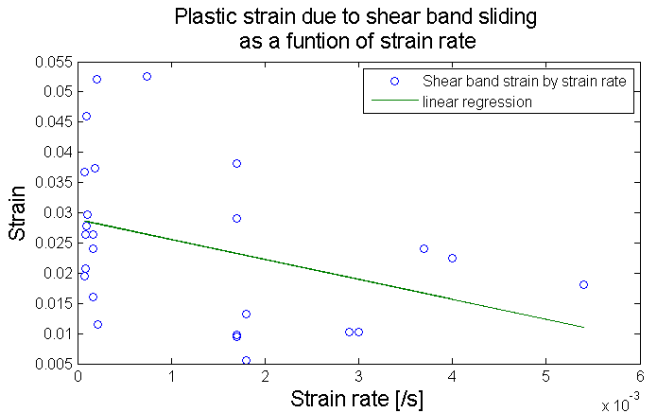

Figure 4.21: Plastic strain from shear band sliding as a function of strain rate.

4.5 XRD

X-ray diffraction was performed on all samples used for tensile testing. Out of all the samples, only three were found to be partially crystalline. The relevant diffractograms, as well as one for a purely amorphous sample, are presented in figure 4.22.

All identified partially crystalline samples showed a strongly reduced shear band sliding distance, when compared to samples at equivalent testing temperatures and strain rates. There was however no conclusive trend observed regarding maximum stress.

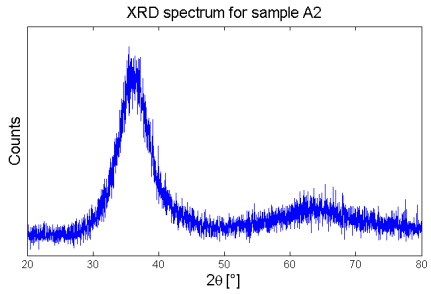

(a) Purely amorphous sample

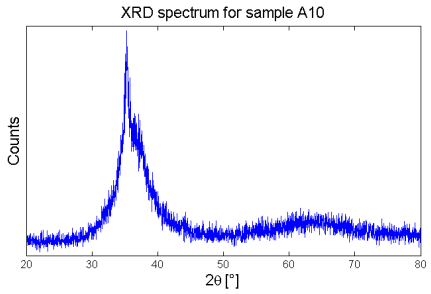

(b) Partially crystalline 1

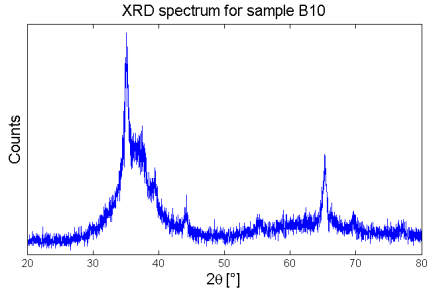

(c) Partially crystalline 2

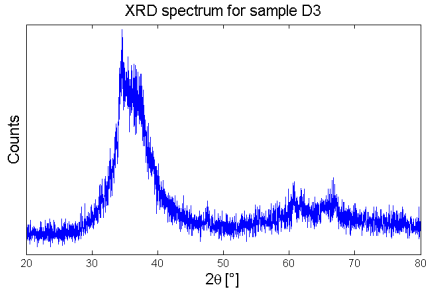

(d) Partially crystalline 3

Figure 4.22: XRD diffractograms for purely amorphous sample (a) as well as all samples identified as partially crystalline (b,c,d).

Chapter 5

Discussion

5.1 Cast Quality

The production of high quality BMG specimen proved very difficult. Out of the total 70 produced specimen, only 25 were high enough quality to be machined and polished to satisfactory conditions. This gives a success rate of only 36% for the samples initially deemed fit for machining. The production quality and output did however significantly improve over the course of the production period, as the manual tilt casting technique was improved. Output of acceptable rods increased from about 1 per day for the earliest productions to 5 per day for the final 20 rods. In total the production time was close to 10 weeks.

5.2 Ultimate Tensile Strength and Shear Band Sliding

A marked rise in ultimate tensile strength (UTS) is found with a decrease in temperature, as is shown in figure 4.12. At room temperature, an average of 1525 MPa is found, close to the previously reported 1500 MPa [26]. This increases to 1584 MPa at 150 K, and further to 1746 MPa at 77 K.

At 77 K, there is a large scatter of UTS values, which range from 1532 to 1888 MPa. No correlation was found to bad XRD results for these specimen. Possible explanations might be bad surface conditions due to insufficient polishing or pores generated during casting. The amount of noise obtained when

doing XRD scans of BMGs is also extraordinarily high, possibly resulting in some weaker specimen having been overlooked.

While UTS was found to be highest at the lowest temperatures, shear band sliding distance reached a peak at tests done at 150 K. Room temperature tests had an average distance of $68\mu m$, tests at 150 K averaged at $130\mu m$, while tests at 77 K slid only $88\mu m$ on average. This suggests that different factors govern the potential for shear band propagation at high and low temperatures.

By reducing the global temperature, heat generated from deformation will dissipate more readily, thereby suppressing a decrease in viscosity. This increases the required stress for shear bands to activate, essentially extending the elastic domain of the specimen, and giving a higher UTS. The fast dissipation of heat also allows the shear band to propagate more slowly once activated, due to the difficulty of reaching critically low viscosity for rupture.

Actual rupture after shear band sliding, will happen when viscosity is sufficiently low, or a sufficient amount of free volume has been generated in the band. Very low temperatures could be conductive to the generation of free volume, possibly through embrittlement of short range atomic structure.

The original goal of this work was to investigate the possibility of a set activation energy in the form of an Arrhenius relation for shear band propagation. The present data is however insufficient to find such a relation, due to the presence of several limiting mechanisms.

5.3 Plasticity

Plastic strain was calculated by trigonometry from measured shear band sliding distance, as shown in section 4.4. While these calculations show some plasticity even at room temperature, this was not present in the provided stress-strain relations shown in section 4.2. This is due to the fact that the shear band sliding speed at room temperature is so high, that it is not observable at the used sampling rate of 10 milliseconds. It can therefore be argued that this does not qualify as plastic strain, but rather simply as crack propagation. Due to the rapid evolution of heat during this deformation at room temperature, the reduction of viscosity in the shear band is presumably large enough to facilitate fracture only by releasing the stress of the internal elastic strains in the specimen. Contrary to the propagation at low temperature, this plastic deformation thereby becomes spontaneous as soon

as critically low viscosity is reached.

Shear band sliding distance also increased at lower strain rates as per figure 4.19. Where energy dissipation was limiting to spontaneous rupture at low temperature, the low energy supply rate is now presumably the limiting factor. By very carefully approaching the UTS of the material, energy is not supplied fast enough for the viscosity to become critically low, before a significant reduction in area has happened.

5.4 Young's Modulus

The Young's modulus was investigated as a function of temperature and strain rate. Based on figures 4.11 and 4.13, the value of E decreases slightly with decreased temperature and strain rate. There is however significant scatter in the data, making the trends uncertain.

Chapter 6

Conclusions and Further Work

An increase in plastic deformation through shear band propagation as a result of lowered temperatures was found. Maximum propagation length happened at the middle temperature 150 K, rather than the lowest 77 K, resulting in the conclusion that there is a shift in limiting mechanisms somewhere between 77 K and 295 K. This shift was proposed to be from heat dissipation rate as a limiting factor to embrittlement of short range structured atoms nucleating rupture.

Due to limits in the precision of temperature and effective strain rate control, no precise relations can be made between temperature, strain rate, UTS and plasticity. General trends of increased UTS and increased plasticity with both lowered temperature and strain rate were however observed. It was therefore proposed that low temperature suppresses the formation of shear bands by dissipating heat from deformation, and thereby keeping viscosity high. This results in elastic deformations up to higher stress levels at lower temperatures. At low strain rates, reduced energy input for the propagation of shear bands was proposed as the limiting mechanism.

In order to fully understand the relations which were investigated in this project, the experiments should be repeated with better controlled temperatures and strain rates. More temperature ranges should be investigated in order to find the true optimal point for shear band sliding distance.

A deeper analysis of the fracture morphology of the tensile specimen could also help shed light on the proposed rupture nucleation from embrittlement at low temperatures.

Appendices

Appendix A

Empirical Temperature Relation

Presented here is the empirical relation between sample holder temperature and actual sample temperature for tensile tests suspended directly above liquid nitrogen. This relation, as shown in figure A.1, was used to calculate the actual sample temperatures for all the tensile tests at 150 K.

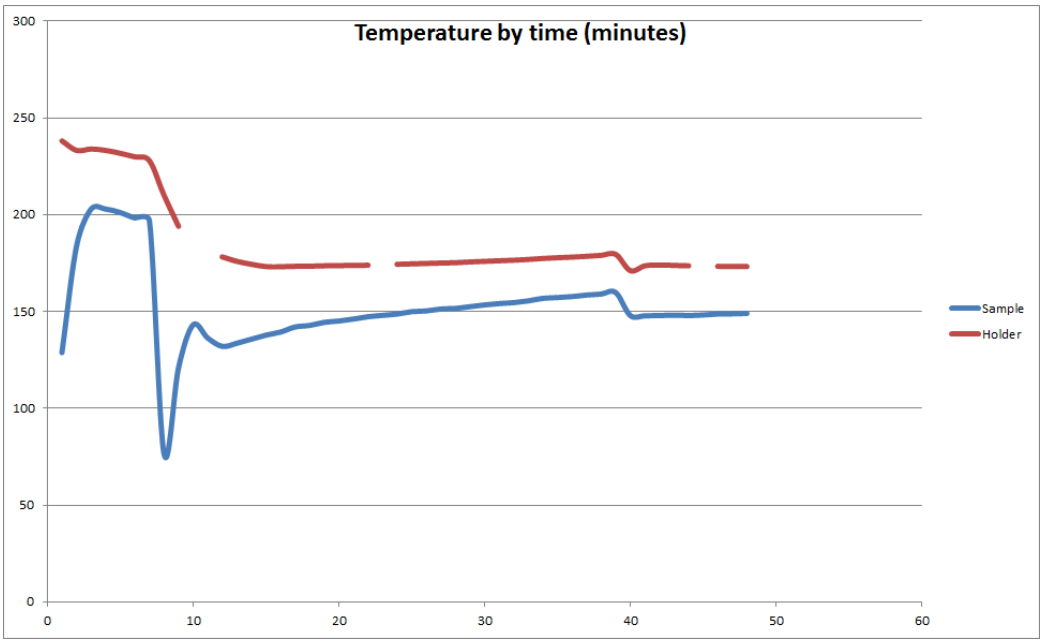

Figure A.1: Temperature for sample and sample holder as a function of time, for tensile tests suspended above liquid nitrogen.

Appendix B

TEMA Motion Tracking

Presented here are screen shots from the TEMA video analysis software. Figure B shows the full program window, including the video, with marked tracking points and distances to be measured, and the tabulated results from the motion tracking (right). Figure **??** shows the final frame of the analysed video, with marked tracking points.

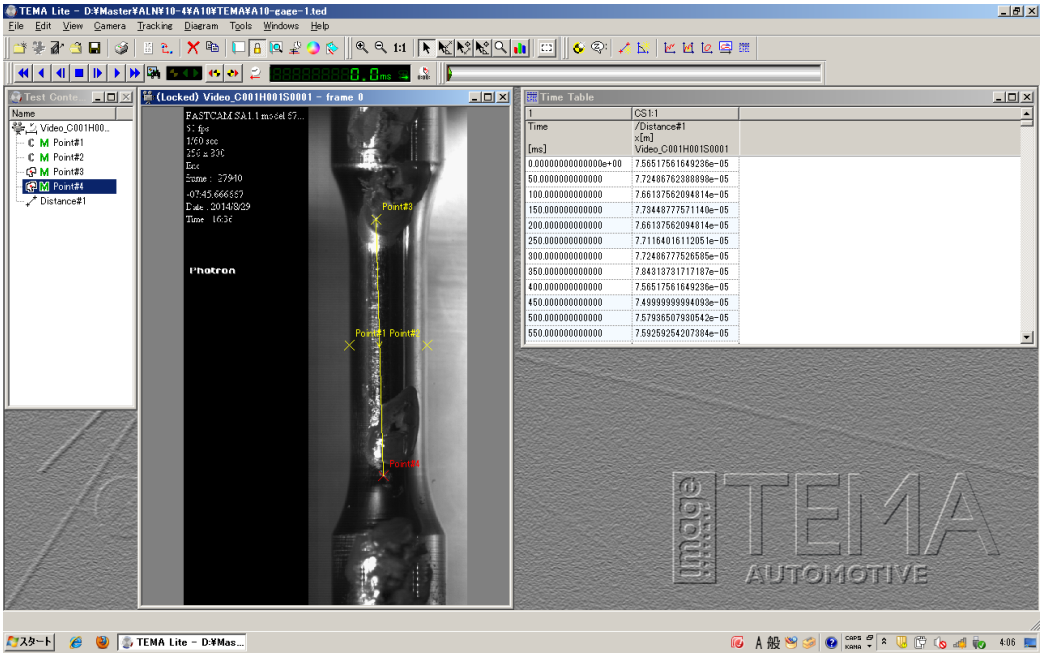

Figure B.1: Screen shot from TEMA video analysis software.

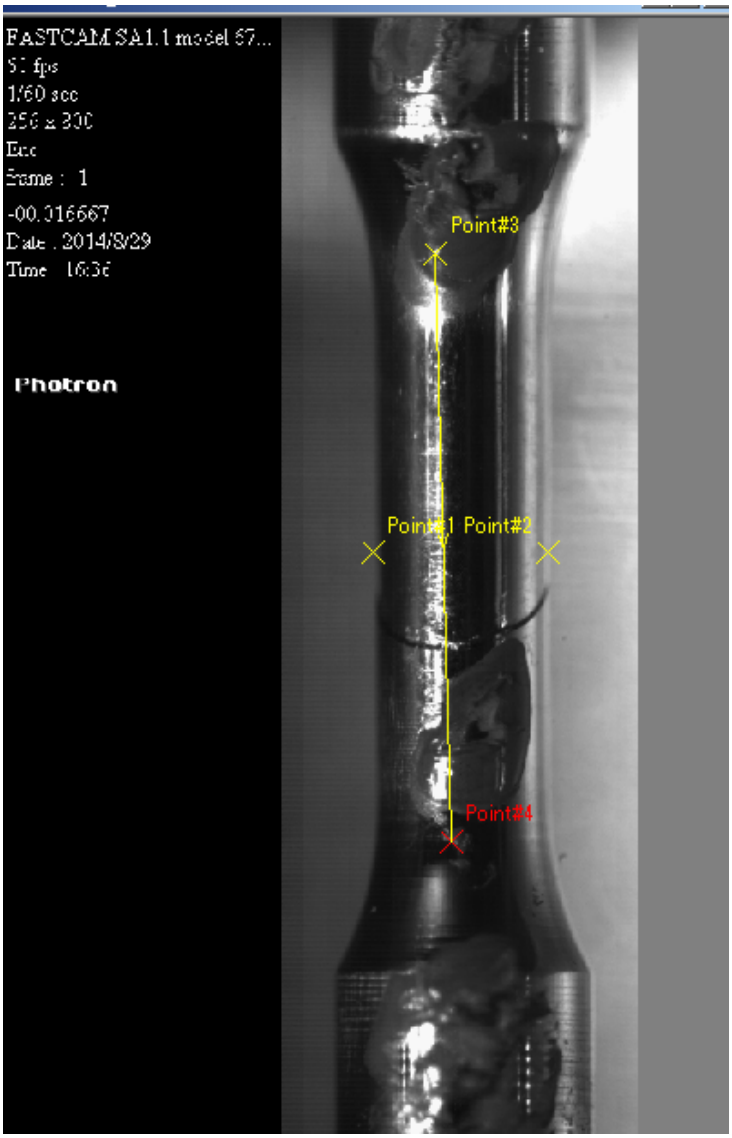

Figure B.2: The analysed video in TEMA, right before fracture.

Bibliography

[1] W. KLEMENT, R. H. WILLENS, and POL DUWEZ. Non-crystalline structure in solidified gold-silicon alloys. *Nature*, 187(4740):869–870, September 1960.

[2] H. B. Lou, X. D. Wang, F. Xu, S. Q. Ding, Q. P. Cao, K. Hono, and J. Z. Jiang. 73 mm-diameter bulk metallic glass rod by copper mould casting. *Applied Physics Letters*, 99(5):–, 2011.

[3] Y. Yokoyama, K. Fujita, A.R. Yavari, and A. Inoue. Malleable hypoeutectic zr–ni–cu–al bulk glassy alloys with tensile plastic elongation at room temperature. *Philosophical Magazine Letters*, 89(5):322–334, April 2009.

[4] D D E Brennhaugen. Production of zr70ni16cu6al8 bulk metallic glasses. Master's thesis, NTNU, Tohoku University, 2014.

[5] Yoshihiko Yokoyama, Kiyohiro Inoue, and Kenzo Fukaura. Pseudo float melting state in ladle arc-melt-type furnace for preparing crystalline inclusion-free bulk amorphous alloy. *Materials Transactions*, 43(9):2316–2319, 2002.

[6] H.S Chen and D Turnbull. Formation, stability and structure of palladium-silicon based alloy glasses. *Acta Metallurgica*, 17(8):1021–1031, August 1969.

[7] Srikanth Sastry. The relationship between fragility, configurational entropy and the potential energy landscape of glass-forming liquids. *Nature*, 409(6817):164–167, January 2001.

[8] Y. Li, S. C. NG, Z. P. LU, Y. P. Feng, and K. Lu. Separation of glass transition and crystallization in metallic glasses by temperature-

modulated differential scanning calorimetry. *Philosophical Magazine Letters*, 78(3):213–220, September 1998.

[9] M.F. Ashby and A.L. Greer. Metallic glasses as structural materials. *Scripta Materialia*, 54(3):321–326, February 2006.

[10] Yoshihiko Yokoyama, Hitoo Tokunaga, Alain Reza Yavari, Masahiro Yamada, Tohru Yamasaki, Kazutaka Fujita, and Akihisa Inoue. Viscous flow in sliding shear band formed during tensile deformation of hypoeutectic zr-based metallic glass. *Intermetallics*, 19(11):1683–1687, November 2011.

[11] Z.P. Lu and C.T. Liu. A new glass-forming ability criterion for bulk metallic glasses. *Acta Materialia*, 50(13):3501–3512, August 2002.

[12] H.J. Willy, L.Z. Zhao, G. Wang, and Z.W. Liu. Predictability of bulk metallic glass forming ability using the criteria based on characteristic temperatures of alloys. *Physica B: Condensed Matter*, 437(0):17–23, March 2014.

[13] Guo-Hua Zhang and Kuo-Chih Chou. A criterion for evaluating glass-forming ability of alloys. *Journal of Applied Physics*, 106(9):–, 2009.

[14] Michiaki Yamasaki, Shinya Kagao, and Yoshihito Kawamura. Thermal diffusivity and conductivity of zr55al10ni5cu30 bulk metallic glass. *Scripta Materialia*, 53(1):63–67, July 2005.

[15] H S Chen. Glassy metals. *Reports on Progress in Physics*, 43(4):353–, 1980.

[16] A. Inoue and A. Takeuchi. Recent development and application products of bulk glassy alloys. *Acta Materialia*, 59(6):2243–2267, April 2011.

[17] O.N. Senkov and D.B. Miracle. A topological model for metallic glass formation. *Journal of Non-Crystalline Solids*, 317(1–2):34–39, March 2003.

[18] Akihisa Inoue, Tao Zhang, and Tsuyoshi Masumoto. Glass-forming ability of alloys. *Journal of Non-Crystalline Solids*, 156–158, Part 2(0):473–480, May 1993.

[19] Y. He, G.M. Dougherty, G.J. Shiflet, and S.J. Poon. Unique metallic glass formability and ultra-high tensile strength in al-ni-fe-gd alloys. *Acta Metallurgica et Materialia*, 41(2):337–343, February 1993.

[20] Douglas C. Hofmann, Jin-Yoo Suh, Aaron Wiest, Gang Duan, Mary-Laura Lind, Marios D. Demetriou, and William L. Johnson. Designing metallic glass matrix composites with high toughness and tensile ductility. *Nature*, 451(7182):1085–1089, February 2008.

[21] P.E. Donovan. A yield criterion for pd40ni40p20 metallic glass. *Acta Metallurgica*, 37(2):445 – 456, 1989.

[22] H.J. Leamy, T.T. Wang, and H.S. Chen. Plastic flow and fracture of metallic glass. *Metallurgical Transactions*, 3(3):699–708, 1972.

[23] Z. F. Zhang, G. He, J. Eckert, and L. Schultz. Fracture mechanisms in bulk metallic glassy materials. *Phys. Rev. Lett.*, 91:045505, Jul 2003.

[24] X. K. Xi, D. Q. Zhao, M. X. Pan, W. H. Wang, Y. Wu, and J. J. Lewandowski. Fracture of brittle metallic glasses: Brittleness or plasticity. *Phys. Rev. Lett.*, 94:125510, Apr 2005.

[25] H. Bei, S. Xie, and E. P. George. Softening caused by profuse shear banding in a bulk metallic glass. *Phys. Rev. Lett.*, 96:105503, Mar 2006.

[26] Yoshihiko Yokoyama, Hitoo Tokunaga, AlainReza Yavari, Toru Kawamata, Tohru Yamasaki, Kazutaka Fujita, Kazumasa Sugiyama, PeterK. Liaw, and Akihisa Inoue. Tough hypoeutectic zr-based bulk metallic glasses. *Metallurgical and Materials Transactions A: Physical Metallurgy and Materials Science*, 42(6):1468–1475–, 2011.

[27] Hitoo Tokunaga, Kazutaka Fujita, and Yoshihiko Yokoyama. Tensile plastic deformation behavior of zr70ni16cu6al8 bulk metallic glass at cryogenic temperature. *Materials Transactions*, 53(8):1395–1399, 07 2012.

[28] Yoshihiko Yokoyama. Schematic illustration of arc-tilt casting method. Webpage: http://www.arcmg.imr.tohoku.ac.jp/en/topics/yokoyama.html, 02 2014.